communications biology

A Nature Portfolio journal

Article

https://doi.org/10.1038/s42003-025-09097-2

Endothelial senescence drives intrinsic skin aging via the neuroimmune CGRP-mast cell axis in mice

Satrio Adi Wicaksono[1,2,3], Gusty Rizky Teguh Ryanto[1], Yoko Suzuki[1], Tetsuya Hara[1,2], Koji Ikeda[4,5], Takeshi Fukumoto[6], Ken-Ichi Hirata[2], Hiromasa Otake[2] & Noriaki Emoto[1,2]

Aging is accompanied by progressive vascular dysfunction, but its effects on skin aging remain poorly understood. Although endothelial cell (EC) senescence is implicated in various age-related diseases, its specific role in dermal aging remains unclear. Here we show that EC senescence contributes to intrinsic skin aging through immune dysregulation. Using an EC-specific senescent mouse model, we observe mast cell activation driven by the neuropeptide calcitonin gene-related peptide (CGRP), independent of traditional IgE-mediated pathways. Senescent ECs secreted pro-inflammatory senescence-associated secretory phenotype (SASP) factors, activating dermal neurons to produce CGRP, leading to mast cell degranulation and subsequent skin aging phenotypes. Pharmacological stabilization of mast cells or inhibition of the EC-SASP-CGRP pathway significantly attenuate dermal thinning, collagen degradation, and delayed wound healing, which are hallmarks of intrinsic skin aging. These findings identify vascular senescence as an upstream regulator of skin aging through a neuroimmune mechanism and suggest potential therapeutic targets for age-related skin deterioration.

Aging is an inevitable biological process characterized by a progressive decline in organ and tissue function[1]. The vascular system plays a crucial role in systemic aging by regulating oxygen and nutrient delivery, immune surveillance, and tissue repair[2,3]. Endothelial cells (ECs), lining the inner surfaces of blood vessels, are particularly vulnerable to senescence, a state of irreversible cell cycle arrest triggered by telomere dysfunction, oxidative stress, and chronic inflammation[3–5]. Senescent ECs secrete a senescence-associated secretory phenotype (SASP), a pro-inflammatory mix of cytokines, chemokines, and matrix-degrading enzymes that disrupt tissue homeostasis and propagate senescence[4–9]. Although EC senescence has been implicated in age-related pathologies such as neurodegeneration, metabolic disorders, and pulmonary dysfunction, its contribution to skin aging remains poorly understood[10–12].

Skin aging is classified into two distinct types: extrinsic aging, driven primarily by environmental stressors such as ultraviolet (UV) radiation and pollution, and intrinsic (chronological) aging, mediated largely by genetic, metabolic, and vascular factors[13–15]. While extrinsic aging manifests as epidermal hyperplasia, elastosis, and pigmentation, intrinsic aging is characterized by dermal thinning, collagen degradation, and impaired wound healing[16,17]. Given the high vascular density within the dermis, microvascular dysfunction may contribute significantly to intrinsic skin aging by disrupting tissue homeostasis[18,19]. However, the precise molecular mechanisms underlying the relationship between vascular dysfunction and intrinsic skin aging remain unknown.

Additionally, aging is associated with chronic low-grade inflammation, termed "inflammaging," which contributes to immune system dysregulation[20,21]. Mast cells, key components of the innate immune system, are abundant in the dermis and essential for tissue remodeling, wound healing, and allergic inflammation[22,23]. Although mast cell degranulation is well-established in UV-induced extrinsic skin aging, its role in intrinsic aging remains largely unexplored despite evidence of increased mast cell activation in aged skin[24,25]. Notably, mast cells can be activated through non-IgE-dependent pathways, suggesting alternative mechanisms may be critical in aging skin[26–29].

In the present study, we investigated whether vascular endothelial senescence contributes to intrinsic skin aging via immune dysregulation, specifically through mast cell activation. Using EC-specific progeroid mouse models, we demonstrated that senescent ECs disrupt dermal immune

[1]Laboratory of Clinical Pharmaceutical Science, Kobe Pharmaceutical University, Higashinada, Kobe, Japan. [2]Division of Cardiovascular Medicine, Department of Internal Medicine, Kobe University Graduate School of Medicine, Chuo, Kobe, Japan. [3]Department of Histology and Cell Biology, Faculty of Medicine, Public Health and Nursing, Universitas Gadjah Mada, Yogyakarta, Indonesia. [4]Department of Cardiovascular Medicine, Kyoto Prefectural University of Medicine, Kamigyou, Kyoto, Japan. [5]Department of Epidemiology for Longevity and Regional Health, Kyoto Prefectural University of Medicine, Kamigyou, Kyoto, Japan. [6]Division of Dermatology, Department of Internal Related, Kobe University Graduate School of Medicine, Kobe, Japan. e-mail: emoto@kobepharma-u.ac.jp

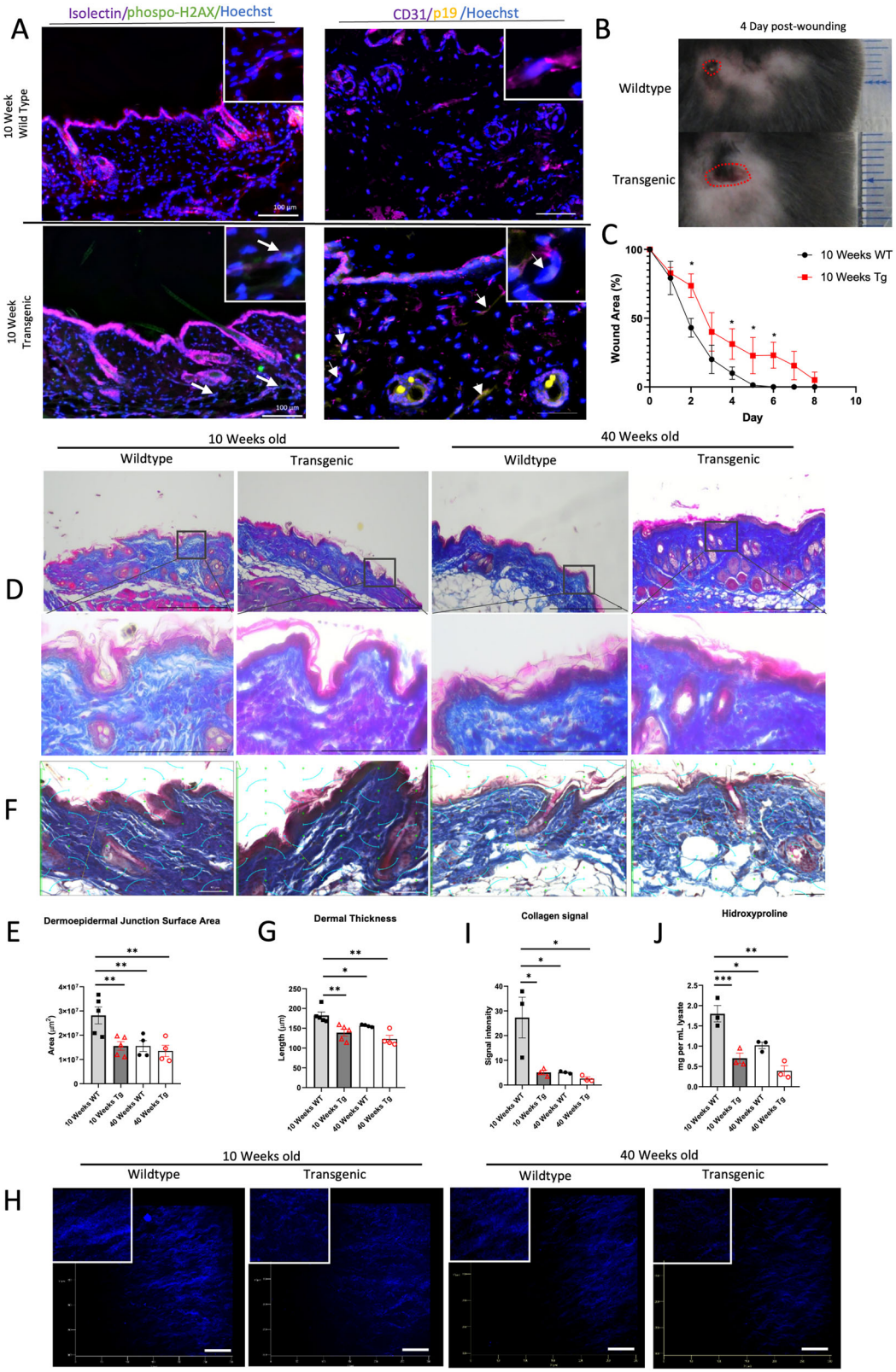

homeostasis through a novel vascular-neuroimmune signaling axis. We identified a mechanism whereby senescent EC-derived SASP factors activate dermal neurons, increasing secretion of calcitonin gene-related peptide (CGRP), which subsequently triggers mast cell degranulation and accelerates skin aging. Furthermore, pharmacological inhibition of mast cell activation or CGRP signaling significantly mitigated skin aging markers, reinforcing the importance of this pathway. These findings establish a direct mechanistic link between vascular aging, neuroimmune activation, and intrinsic skin aging, highlighting potential therapeutic targets for mitigating age-related skin deterioration.

Fig. 1 | Vascular senescence alters dermal morphology and impairs wound healing. A Confirmation of endothelial senescence in the dorsal skin of 10-week-old TRF2DN-Tg. White arrows represent the colocalization of the respective endothelial markers with cellular senescence markers. **B** Representative images of the wound healing challenge on day 5 showing an almost healed wound in wild-type (WT) mice (left image) and an open wound in 10-week-old TRF2DN mice (right image). **C** Quantitative graph of wound healing challenge over time. Data were compared with the initial wound area on day 0 ($n = 5$ each). **D** Representative images of Masson's trichrome staining in WT and Tg mice at 10 and 40 weeks of age. Changes in the dermoepidermal junction were observed at higher magnification. Low magnification scale bar = 360 μm, high magnification scale bar = 131.462 μm. **E** Quantification of the dermoepidermal junction surface area of either 10- and 40-week-old WT or Tg mice ($n = 4$–5 each). **F** Representative image of stereological cycloid usage for dermo-epidermal junction and dermal thickness measurements at random intersection points between green cycloids, with the dermoepidermal junction measured perpendicular to the DEJ plane. **G** Quantification of dermal thickness in 10 & and 40-week-old mice. **H** Representative image of intravital dermal collagen observation using second-harmonic generation modality. Scale bar = 100 μm. **I** Quantification of dermal collagen intensity through the second-harmonic generation of either 10- and 40-week-old WT or Tg mice ($n = 3$ each). **J** Dermal collagen content was confirmed using a hydroxyproline assay in WT and Tg mice at 10- and 40-week time points ($n = 4$ each). Data are presented as mean ± SEM. Two-way analysis of variance (ANOVA) with Tukey's post hoc test was used to analyze the differences between three or more groups. #$P < 0.0001$; ***$P < 0.001$; **$P < 0.01$; *$P < 0.05$. Not significant ($P > 0.05$).

Results

Vascular senescence alters dermal morphology and impairs wound healing

Our laboratory recently generated mice overexpressing a dominant-negative form of telomeric repeat-binding factor 2 (TRF2DN) under the control of vascular endothelial cadherin (VE-cadherin; VEcad) promoter to specifically induce EC senescence. Previously, we demonstrated senescent EC presence in the lungs, leading to exacerbated pulmonary hypertension, and in adipose tissue, resulting in impaired metabolic regulation[10,12]. To verify EC senescence in the skin, we assessed senescence markers using immunostaining. Co-localization of Isolectin-B4, a marker for microvascular ECs, with phospho-H2AX, indicating senescence-associated DNA damage, confirmed endothelial senescence in dermal tissues of Tg mice (Fig. 1A). Additional co-localization studies using alternative endothelial markers, CD31 and p19 as cell-cycle arrest marker, further supported the EC-specific senescence in Tg mice (Fig. 1A).

Considering previous reports that vascular endothelial senescence induces aging in various organs[10], we hypothesized that similar-associated changes may also occur in the skin[10]. To test this hypothesis, we assessed skin aging phenotypes through analyses of morphology, collagen content, and wounding healing capacity. First, we used a skin punch biopsy model and observed wounds in Tg mice remained prominent at a time point when corresponding wounds in WT mice were almost healed (Fig. 1B). Quantitative analysis confirmed a significantly reduced wound healing rate in Tg mice relative to WT counterparts (Fig. 1C).

Next, we performed histological analysis to examine structural changes in the skin. The dermoepidermal junction (DEJ) in dorsal skin samples from Tg mice at 10 and 40 weeks of age appeared notably flatter that in age-matched WT controls, as quantitatively reflected by significantly reduced DEJ surface areas (Fig. 1D, E). Masson's trichrome staining and a significantly thinner dermal layer in the skin of EC-progeria mice (Fig. 1F, G). In line with these results, intravital imaging via second-harmonic generation (SHG) two-photon microscopy demonstrated significantly reduced dermal collagen signal intensity in 10-week-old Tg mice, comparable to both older mice (40-week-old WT and Tg mice) (Fig. 1H, I). The decreased collagen content was further confirmed by hydroxyproline assay, which showed significantly reduced collagen content in 10-week-old Tg mice (Fig. 1J). These findings suggest that endothelial cell senescence alters dermal morphology and impairs wound healing capacity.

Cellular Aging occurs in vascular senescent dorsal skin

Senescence-driven tissue aging has traditionally been delineated with changes in several parameters, including reduced proliferation, cell cycle arrest, increased DNA damage response, and expression of senescence associated secretory phenotype (SASP). We next tried to confirm those changes in the skin of Tg mice[30]. We first evaluated the proliferation marker Ki67 by immunostaining. Quantification showed significantly fewer Ki67$^+$ proliferating cells in Tg mouse skin compared to WT mice (Fig. 2A, B). Furthermore, the number of cells positive for phospho-H2AX, indicative of an activated DNA damage response, was significantly higher in both the dermal and epidermal layers of dorsal skin from Tg mice (Fig. 2C, D). Analysis of the senescence marker SA-β-Gal also revealed a significantly higher number of positive cells in both skin layers of 10-week-old Tg mice, a pattern that was also observed in older animals (Fig. 2E, F). Quantitative real-time PCR analysis demonstrated higher expression of the CDK inhibitors (cell cycle arrest markers) *p19* and *p21* in both the epidermis and dermis (Fig. 2G). Immunoblotting of whole skin lysates similarly revealed elevated protein levels of p19. Additionally, enhanced phosphorylation of ERK1/2 (pERK1/2) and increased activation of its downstream target NFκB were observed in Tg mouse skin (Fig. 2H, I). Consistent with these findings, gene expression of the SASP-associated cytokines interleukin (*IL) 1-α, IL 1-β*, and *IL-6* was higher in the Tg dermis, while only *IL-1β* was significantly higher in the epidermis (Fig. 2G). We further assessed the expression of additional skin-related growth factors and genes associated with aging. Expression of fibroblast growth factor 2 (*FGF2*) was substantially reduced in the dermis, whereas *FGF1* was elevated in both epidermal and dermal layers (Supplementary Fig. S1A). Immunostaining revealed colocalization of phospho-H2AX and S100A4 in Tg mice, thereby supporting the notion of fibroblast aging in Tg mice (Fig. 2J). Additionally, expression of the anti-aging gene Sirtuin 2(*SIRT2*) was significantly decreased in the epidermis, and endothelin 1 (*Edn1*), a proinflammatory gene, was significantly increased in the dermis of Tg mice (Supplementary Fig. 1A). To evaluate the structural and molecular integrity of the vasculature in Tg mice, we examined the dermal vasculature through immunostaining and intravital imaging. The vascular area fraction in Tg dermal mice was comparable to that in their WT counterparts (Supplementary Fig. S1B, C), in line with the intravital observation of dermal vessel density by two-photon microscopy (Supplementary Fig. 1D). Further, gene expression of *HIF-1α* was also comparable between groups in both skin layers (Supplementary Fig. S1E), confirming that EC-specific genetic modifications did not alter dermal vasculature anatomy. Our data suggest that skin aging in EC-specific progeroid mice occurs at both cellular and organ levels, with more pronounced alterations observed in the dermal layer.

Attenuation of skin aging phenotype via stabilization of non-IgE-dependent mast cell degranulation

As SASP-mediated inflammation was markedly elevated in Tg dorsal skin, we hypothesized that innate immune cells might be present in the dermis and sought to test this further. Notably, although cell density and transcriptional levels of NIMPR14$^+$ neutrophils (Supplementary Fig. S2A, B) and F4/80$^+$ macrophages (Supplementary Fig. S2C, D) were comparable between groups, we observed significantly increased mast cell density in the dermal layer of 10-week-old Tg mice compared to WT controls (Fig. 3A, C). Similar results were noted in 40-week-old Tg mice (Fig. 3A, C). Closer examination revealed a significantly higher number of activated, degranulated mast cells in the EC-specific progeria mouse groups at both 10 and 40 weeks compared to their respective WT counterparts (Fig. 3B, D). Tryptase immunostaining revealed increased tryptase$^+$ cells in Tg mice with a morphology of cytoplasmic exteriorization, a characteristic of degranulated cells (Supplementary Fig. S3A, S3B), confirming the mast cell degranulation previously observed through the toluidine blue staining. This phenomenon occurred comparably in both male and female mice comparably within each

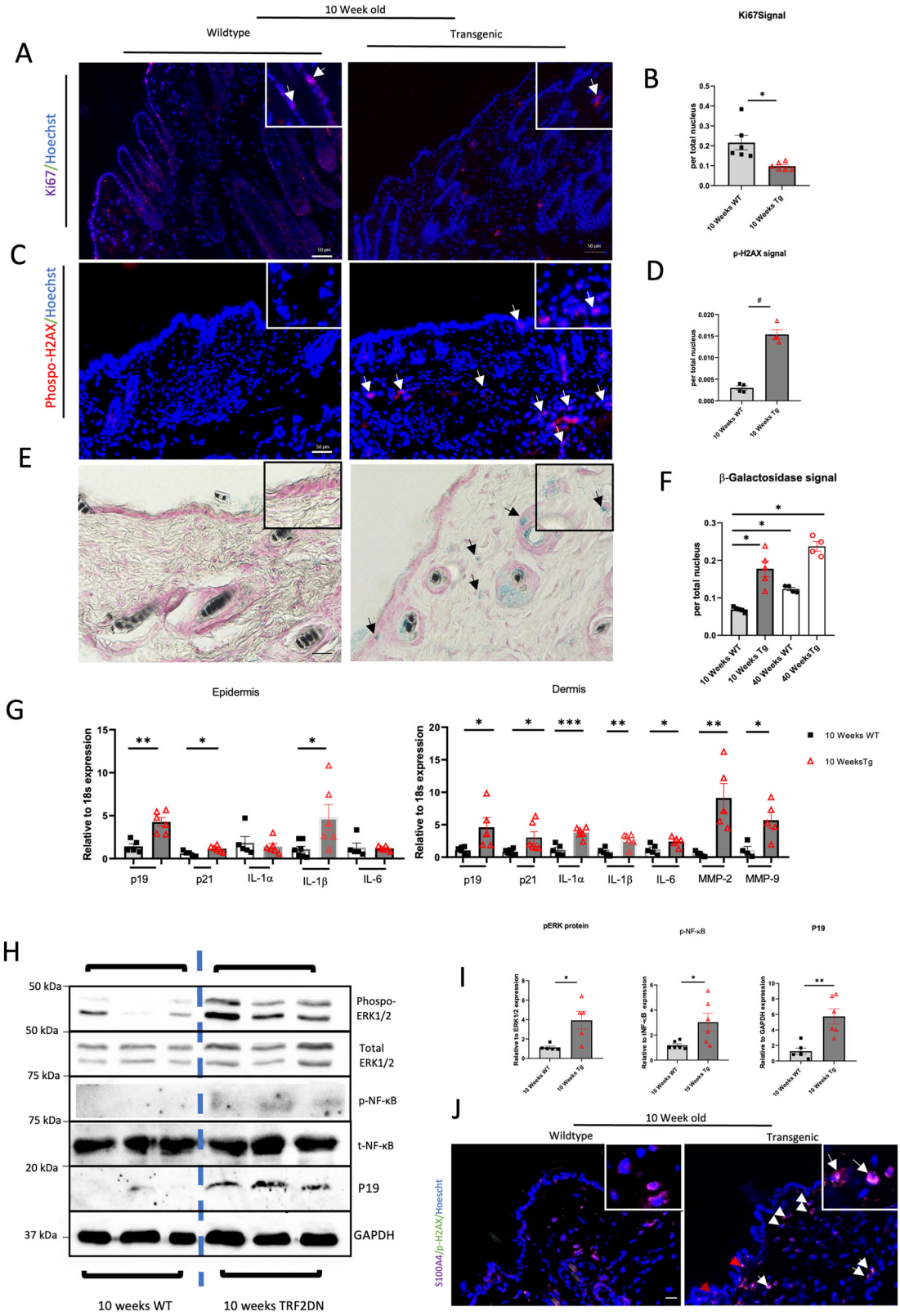

group (Supplementary Fig. S3C). To determine whether activated mast cells directly influence skin cell senescence, we performed spatial colocalization studies of the senescence marker β-gal with the mast cell marker CD117 (c-kit) using immunostaining. Notably, c-kit$^+$ mast cells were located in close proximity, but did not directly co-localize, with β-gal$^+$ senescent cells in the dermis of Tg mice (Fig. 3F white arrow). We also observed c-kit$^+$ cells residing close to the epidermis (Fig. 3F red arrow). Mast cells are typically involved in IgE-mediated allergic reactions[23]; however, serum IgE levels did not differ significantly between 10-week-old WT and Tg mice (Fig. 3E), suggesting mast cell activation occurs independently of IgE-mediated mechanisms. Collectively, these findings indicate non-IgE-dependent mast cell activation in aged skin from EC-specific progeria mice.

Fig. 2 | Cellular Aging occurs in the vascular senescent dorsal skin. **A** Representative image of immunofluorescence staining for Ki67$^+$ proliferating cells in the dorsal skin of WT or Tg 10-week-old mice. **B** Quantification of Ki67$^+$ cells in the WT and Tg mice relative to the total nucleus ($n = 6$ each). **C** Representative image of immunofluorescence staining for the DNA-Damage response marker phospho-H2AX$^+$ cells. Positive cells are indicated by white arrows. **D** Quantification of phospo-H2AX$^+$ cells in WT and Tg mice relative to the total nucleus ($n = 4$ each). **E** Representative images of X-gal staining to detect the expression of senescence-associated beta-galactosidase in WT and Tg mice. The expressing cells are indicated by black arrows. **F** Quantification of SA-β-Gal$^+$ cells relative to total nucleus ($n = 4–5$ each). Scale bar = 50 μm. **G** Transcription level analysis of CDK inhibitors and SASP factors in the dermis and epidermis of either WT or Tg 10-week-old mice using RT-qPCR ($n = 5–6$ each). **H** Representative immunoblotting for pERK 1/2, p-NFκB, and P19 expression of whole skin lysate epidermis of either WT or Tg 10-week-old mice. **I** Densitometry quantification for immunoblotting in (**H**) ($n = 5$ each). **J** Representative immunofluorescence images of S100A4 and the cellular senescence marker Phospo-H2AX. Colocalization in the dermis of 10-week-old Tg mice is indicated by white arrows. Red arrows indicate colocalization in the epidermis. Data are presented as mean ± SEM. A two-tailed Student's t-test was used to analyze the differences between two groups. Two-way analysis of variance (ANOVA) with Tukey's post hoc test was used to analyze the differences between three or more groups. #$P < 0.0001$; ***$P < 0.001$; **$P < 0.01$; *$P < 0.05$. Not significant ($P > 0.05$).

To further evaluate our hypothesis that mast cell activation contributes to the skin aging phenotype, we sought to prevent mast cell degranulation by administering quercetin, a potent mast cell-stabilizer flavonoid[31], intraperitoneally with vehicle administration serving as a control (Fig. 3G). Histological analysis revealed lower mast cell density in the dermis of Tg mice treated with quercetin compared to vehicle-treated Tg mice. Moreover, significantly fewer activated mast cells were detected in quercetin-treated Tg mice, suggesting effective mast cell stabilization by quercetin (Fig. 3H, I). A similar phenotypic analysis confirmed improvement in EC progeria-driven skin aging after quercetin treatment; significantly higher dermal-epidermal junction surface area and a thicker dermis layer in the quercetin-treated Tg groups compared to vehicle-treated counterparts, with value comparable to the WT groups (Fig. 3J, K). Further, expression levels of inflammatory markers were significantly lower in both epidermal and dermal layers following quercetin treatment (Supplementary Fig. S4A). Similar trends were observed in CDK inhibitor markers at transcription and protein levels, along with a slight reduction in ERK 1/2 signaling activation and p19 (Supplementary Fig. S4A–C). We further assessed the reduction of inflammation by serum IL-1β measurement and found a significantly lower expression in quercetin-treated Tg mice (Supplementary Fig. S4D).

To assess the direct effect of senescent ECs on specific skin cells, we isolated and cultured fibroblasts from WT mice and treated them with conditioned media from ECs isolated from Tg or WT. Endothelial cells isolated from 10-week-old TRF2DN mice exhibited significantly elevated expression of CDK inhibitors and SASP factors, including *IL-1α, IL-6, TNF-α*, and *Edn1* (Supplementary Fig. S5A, B). However, fibroblasts exposed to conditioned medium from those TRF2DN endothelial cells exhibited only slight changes in *IL-1α* and *FGF2* expression, with no significant differences observed in *p16, p19*, and *p21* expression (Supplementary Fig. S5C, D). Overall, these findings support the hypothesis that mast cell degranulation is an important player driving the skin aging phenotype and suggest that stabilizing mast cells can attenuate aging-related skin changes in EC-specific progeria mice.

To assess whether quercetin might affect endothelial senescence, we performed immunostaining and observed colocalization of microvascular and cellular senescence markers in both group of Tg mice (Supplementary Fig. S5E). Additionally, increased Edn1 expression observed in EC-specific progeria was unchanged by quercetin treatment (Supplementary Fig. S5F). We also tested quercetin's effects on fibroblast senescence induced by H_20_2 exposure. Notably, p19 expression was lower in H_20_2-treated groups that received quercetin; however, p21 expression was higher even compared to groups treated with H_20_2 only (Supplementary Fig. S5G, H). These data indicate that quercetin neither directly affects fibroblast senescence nor prevents endothelial cell senescence.

Younger TRF2DN-Tg mice showed some skin aging parameters and higher CGRP expression with comparable SASP expression

Next, we sought to identify potential mechanisms responsible for non-canonical mast cell activation observed in the dermal tissue of Tg mice. Interleukins and endothelin-1 (*Edn1*) have been previously reported to induce mast cell degranulation through IgE-independent pathways[27,28]. Notably, both gene expressions were significantly higher in the dermal layer of Tg mice. To explore molecular pathways involved in mast cell activation, we examined Tg mice at an earlier developmental stage (4 weeks). Early signs of skin aging in 4-week-old Tg mice were already observed, demonstrated by a significantly lower DEJ surface area compared to aged-matched WT controls. However, dermal thickness remained comparable between groups (Fig. 4A, B). Furthermore, Tg mice exhibited lower Ki-67 expression levels, whereas phospho-H2AX levels were comparable between Tg and WT groups (Fig. 4C–F). Additionally, we observed significantly higher mast cell density and increased degranulation rates in the skin of 4-week-old Tg mice compared to WT mice (Fig. 4G, H), indicating that mast cells were already activated at this early time point. Notably, transcription-level analysis revealed comparable expression levels of SASP factors between Tg and WT mice at 4 weeks, with only dermal CDKI *p19* expression significantly higher levels in Tg mice (Fig. 4I). Furthermore, at this early stage, expression levels of endothelin ligands and receptors in the dermis were also comparable between the groups (Fig. 4G). Another group of molecules that have been reported to induce mast cell activation neuropeptides, such as calcitonin gene-related peptide (CGRP). Immunoblot analysis of skin samples from 4-week-old Tg mice showed significantly higher CGRP expression and slightly higher activation of NFκB signaling (Fig. 4H). These results suggest that mast cell degranulation precedes the full manifestation of the skin aging phenotype and may be induced by elevated CGRP levels.

High CGRP levels induce mast cell degranulation, and CGRP inhibition alleviates skin aging in 10-week-old TRF2DN-Tg mice

Given the observed CGRP overexpression in 4-week-old Tg mice, we examined whether this phenomenon persisted into later stages. Immunoblotting confirmed persistently elevated CGRP expression in 10-week-old Tg mice compared to WT controls (Fig. 5A, B). In contrast, the transcription level of *Tac1* gene, which encode several neuropeptides such as substance P, neurokinin A, neuropeptide K, and neuropeptide gamma, was comparable between groups, indicating that the activation seen is specifically mediated by CGRP (Fig. 5C)[32,33]. Since CGRP is predominantly produced by neuronal cells[34], we sought to clarify how CGRP expression related to EC-specific senescence processes observed in our mouse model. Using immunostaining, we spatially analyzed the relationship between dermal microvasculature (marked by isolectin-B4$^+$) and nerve cells (marked by synaptophysin$^+$). We observed proximity between these structures (Fig. 5D). Using VE-Cadherin as another marker of endothelial cells, we found similar proximity with synaptophysin$^+$ fiber (Supplementary Fig. S6A). Further immunostaining analyses demonstrated clear co-localization of CGRP with synaptophysin$^+$ axons, but not with CD 117$^+$ mast cells, although these cell types were found adjacent to each other (Fig. 5E). Unilateral surgical axotomy was conducted to test whether CGRP was neuron-derived (Supplementary Fig. S6B, S6C). Significantly lower CGRP expression was observed in denervated Tg Skin (Supplementary Fig. S6D, S6E), confirming dermal neurons as the main source of the excessive neuropeptide. Comparable dermal neuron density between groups from immunostaining observation (Supplementary Fig. S6F, S6G) supported our conclusion that increased neuron activation caused the abundance of CGRP levels instead of a neuronal density increase. These data support a

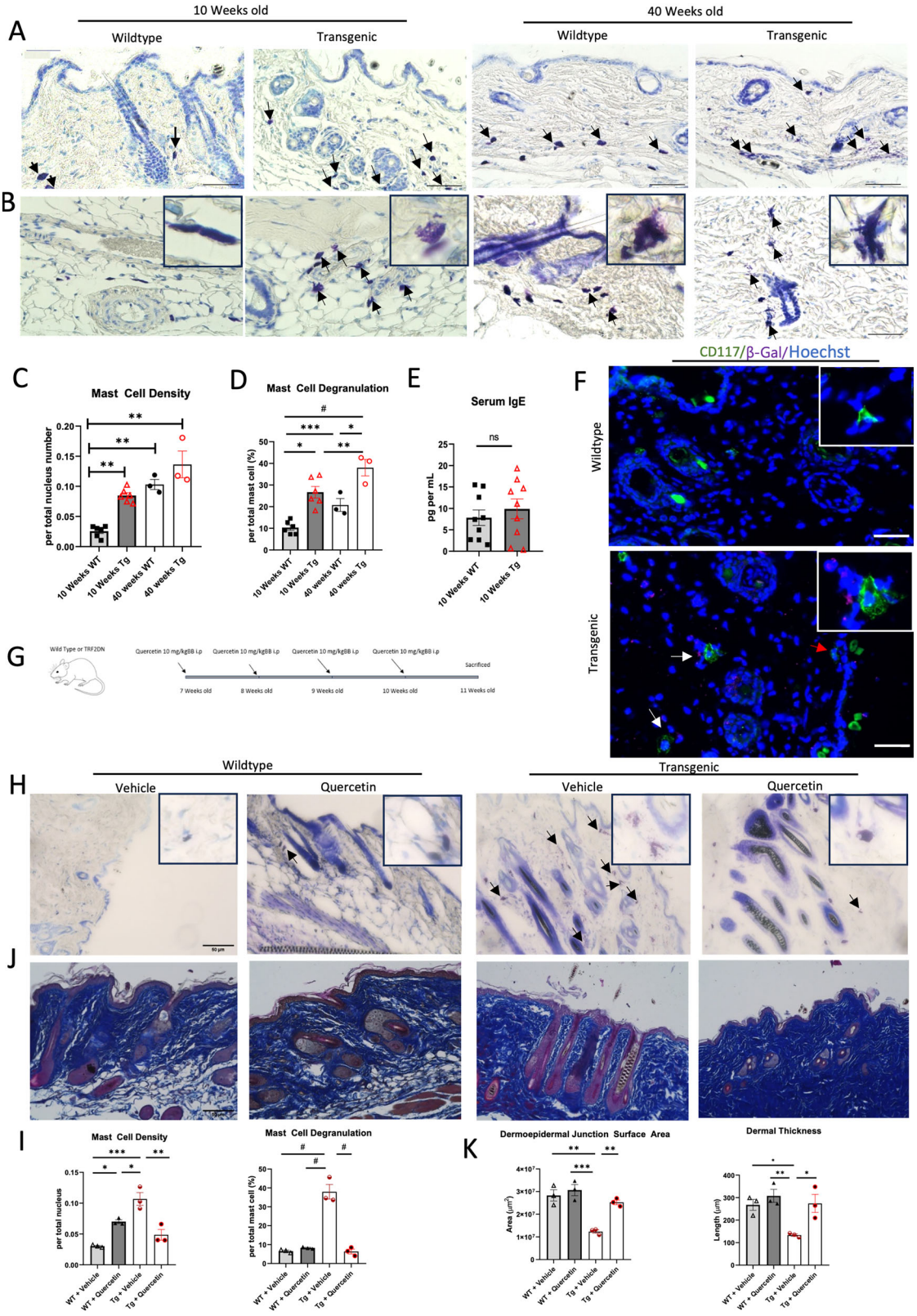

biological plausible mechanism in which EC-specific progeria induces CGRP expression in dermal nerves, subsequently triggering mast cell activation.

To further test our hypothesis that CGRP was responsible for mast cell activation in our model, we attempted to block the CGRP signalling using atogepant, CGRP receptor inhibitor[35], administered intradermally every three days for a total of four doses (Fig. 5E). Because intradermal administration limits the effect locally, we performed atogepant and vehicle treatments on separate dorsal skin areas of the same mice. Although CGRP expression remained elevated in all Tg groups, toluidine blue staining showed that mast cell degranulation rates were significantly lower in the skin area treated with atogepant compared to vehicle-treated areas (Fig. 5F, G).

Fig. 3 | Attenuation of skin aging phenotype via stabilization of non-IgE-dependent mast cell degranulation. A Representative images of toluidine blue staining of WT and Tg mice at 10 and 40 weeks of age. Mast cells are indicated by black arrows. Scale bar = 50 μm. **B** Representative high-power field images of mast cell degranulation observed in WT and Tg mice at 10 and 40 weeks of age. Degranulated mast cells are indicated by black arrows. **C** Quantification of mast cell density in both 10 WT or Tg mice relative to total nuclei ($n = 3–6$ each). **D** Quantification of degranulated mast cells relative to the total mast cell number of either WT or Tg mice in 10 and 40-week-old mice ($n = 3–6$ each). **E** Serum IgE level measurement on both 10-week-old WT and Tg mice ($n = 8–9$ each). **F** Representative image of immunofluorescence staining for c-kit+ mast cell and β-Gal+ senescence cell in both dermis and epidermis of 10-week-old WT and Tg mice. White arrows indicate the close location of both markers in the dermis, and red arrows indicate mast cells lying very close to the epidermis. **G** Mast cell stabilization using quercetin injection schematic. **H** Representative images of toluidine blue-staining in 10-week-old WT and Tg mice that received either quercetin or vehicle. Degranulated mast cells are indicated by black arrows. **I** Representative images of Masson's trichrome staining in 10-week-old WT and Tg mice that received either quercetin or vehicle. **J** Quantification of mast cell density and degranulation (**H**) ($n = 3$ each). **K** Quantification of the dermoepidermal junction surface area and dermal thickness in (**J**) ($n = 3$ each). Data are presented as mean ± SEM. A two-tailed Student's t-test was used to analyze the differences between two groups. Two-way analysis of variance (ANOVA) with Tukey's post hoc test was used to analyze the differences between three or more groups. #$P < 0.0001$; ***$P < 0.001$; **$P < 0.01$; *$P < 0.05$. Not significant ($P > 0.05$).

This improvement was also evident histologically, as demonstrated by the significantly higher dermoepidermal junction surface area observed in the atogepant-treated Tg skin compared to the vehicle-treated skin (Fig. 5G). Mast cell stabilization was further resulted in significantly lower levels of phosphorylated NFκB and senescence marker P19 in atogepant-treated skin (Fig. 5I, J). We confirmed our hypothesis through an ex vivo approach, in which isolated peritoneal-derived mast cells were exposed to conditioned media from WT or TRF2DN endothelial cell isolates, or recombinant CGRP (Supplementary Fig. S6H). Exteriorization of cell morphology was observed mainly in the CGRP-treated group (Supplementary Fig. S6I, S6J). Blotting of collected mast cell media further revealed the absence of CGRP in TRF2DN-EC conditioned media. At the same time, secreted tryptase was only observed in the CGRP-treated group (Supplementary Fig. S6K), highlighting the necessity of the neuropeptide in inducing immune cell activation. Collectively, our findings suggest that elevated CGRP expression from activated dermal neurons causes mast cell degranulation, and CGRP inhibition effectively stabilizes mast cells, followed by attenuation of the skin aging phenotype. Collectively, our findings suggest that elevated CGRP expression from activated dermal neuron causes mast cell degranulation, and CGRP inhibition effectively stabilizes mast cells followed by attenuation of the skin aging phenotype.

SASP from progeroid ECs induces CGRP overexpression, which is attenuated by dexamethasone treatment

To identify EC-derived molecules potentially inducing neuronal CGRP expression, we isolated dermal endothelial cells from young TRF2DN mice. Given that mast cell activation was evident at 4 weeks of age, we investigated molecules expressed by TRF2DN-Tg ECs at an even earlier age (2 weeks). At this early time point, expressions of *IL-1α* and *IL-6* were significantly increased, whereas *Edn1* was significantly reduced and *TNF-α* expression was comparable to controls (Fig. 6A). These findings suggest that EC-derived SASP factors, particularly *IL-1α* and *IL-6*, may induce CGRP expression in dermal neurons in our model. Observation in dorsal root ganglia and sciatic nerve, neuronal tissue with dense and anatomical closeness to vasculature[36,37], revealed significantly higher CGRP expression in Tg mice, supporting our hypothesis that EC-derived molecules activate the neuron (Supplementary Fig. S7A, S7B).

To confirm whether SASP from Tg ECs triggered CGRP secretion and subsequent downstream events contributing to skin aging, we inhibited SASP production by administering daily intraperitoneal injections of dexamethasone (Fig. 6B). Steroid-treated Tg mice had significantly fewer degranulated mast cells compared to vehicle-treated mice (Fig. 6C, D). Histological examination using Masson's trichrome staining indicated amelioration of dermoepidermal junction flattening, reflected by a significantly higher DEJ surface area in dexamethasone-treated Tg mice compared to the vehicle group (Fig. 6E, F). Immunoblotting further supported our hypothesis that SASP induces CGRP expression, as evidenced by significantly reduced CGRP levels in dexamethasone-treated Tg mice. These mice displayed lower activity of the pro-inflammatory regulator NFκB and expression of the CDK inhibitor p16 (Fig. 6G, I). Analyses at transcription-level revealed lower *IL-6* and *TNF-α* expression in dexamethasone-treated Tg mice (Fig. 6I). We further test our hypothesis by administering tocilizumab intradermally to specifically inhibit IL-6 signaling that we identified as a possible culprit SASP in our model (Supplementary Fig. S7C). Attenuation of CGRP expression was observed in the treated-Tg skin area (Supplementary Fig. S7D, E) followed by histological evidence of lower mast cell degranulation accompanied by amelioration of dermo-epidermal junction surface area (Supplementary Fig. S7F, S7G), supporting the role of EC-derived SASP to activate CGRP-releasing neurons.

To assess whether the inhibitors have direct effects on the skin cells, we treated isolated WT fibroblast with atogepant or dexamethasone (Supplementary Fig. 8A). We observed significant higher TNF-α in atogepant-treated group but comparable CDKIs expressions (Supplementary Fig. S8B). Collectively, we concluded that EC-derived SASP could indeed trigger CGRP-mediated mast cell degranulation and accelerate skin aging.

Discussion

Aging leads to progressive tissue dysfunction; however, the precise role of vascular aging in skin homeostasis remains poorly understood. Our study provides direct evidence that vascular endothelial senescence promotes intrinsic skin aging through immune dysregulation, revealing a EC-SASP-CGRP-mast cell signaling axis that links vascular dysfunction to skin deterioration.

We demonstrated that EC-specific progeroid mice exhibited key hallmarks of intrinsic skin aging, including dermal thinning, collagen degradation, and delayed wound healing, closely resembling chronological skin aging in humans[15–17,38]. These findings suggest that vascular aging is not merely a secondary consequence of skin aging but actively drives the aging process by disrupting immune homeostasis[20,30,39]. Although previous studies have demonstrated a role for EC senescence in neurodegeneration and metabolic decline[10,11], our findings extend these observations to skin physiology, highlighting a broader impact of vascular dysfunction on aging.

A major discovery of our study is that mast cell activation in aging skin occurs independently of IgE and is instead mediated by CGRP, a neuropeptide secreted by dermal axons[23,34,40,41]. This observation indicates that vascular aging influences skin physiology through neuroimmune crosstalk, representing a previously unrecognized mechanism in dermatological aging research. Our data demonstrate that senescent ECs release SASP factors, including the cytokines IL-1β and IL-6, activate dermal neurons as previously reported[42,43], leading to sustained CGRP expression and subsequent mast cell degranulation. Although the CGRP-induced mast cell activation has been renowned in the pathophysiology of migraine and trigeminal neuralgia[44,45], its involvement in skin pathology has not been elucidated. Auspiciously, our finding provides a direct mechanistic link between vascular senescence and immune dysregulation in aging skin.

To further validate this mechanism, we performed pharmacological interventions at different points along the EC-SASP-CGRP-mast cell signaling cascade. Mast cell stabilization using quercetin effectively reduced mast cell degranulation and partially mitigated skin aging phenotypes. However, quercetin did not fully reverse fibroblast senescence nor prevent EC dysfunction, suggesting mast cells function as intermediaries rather than

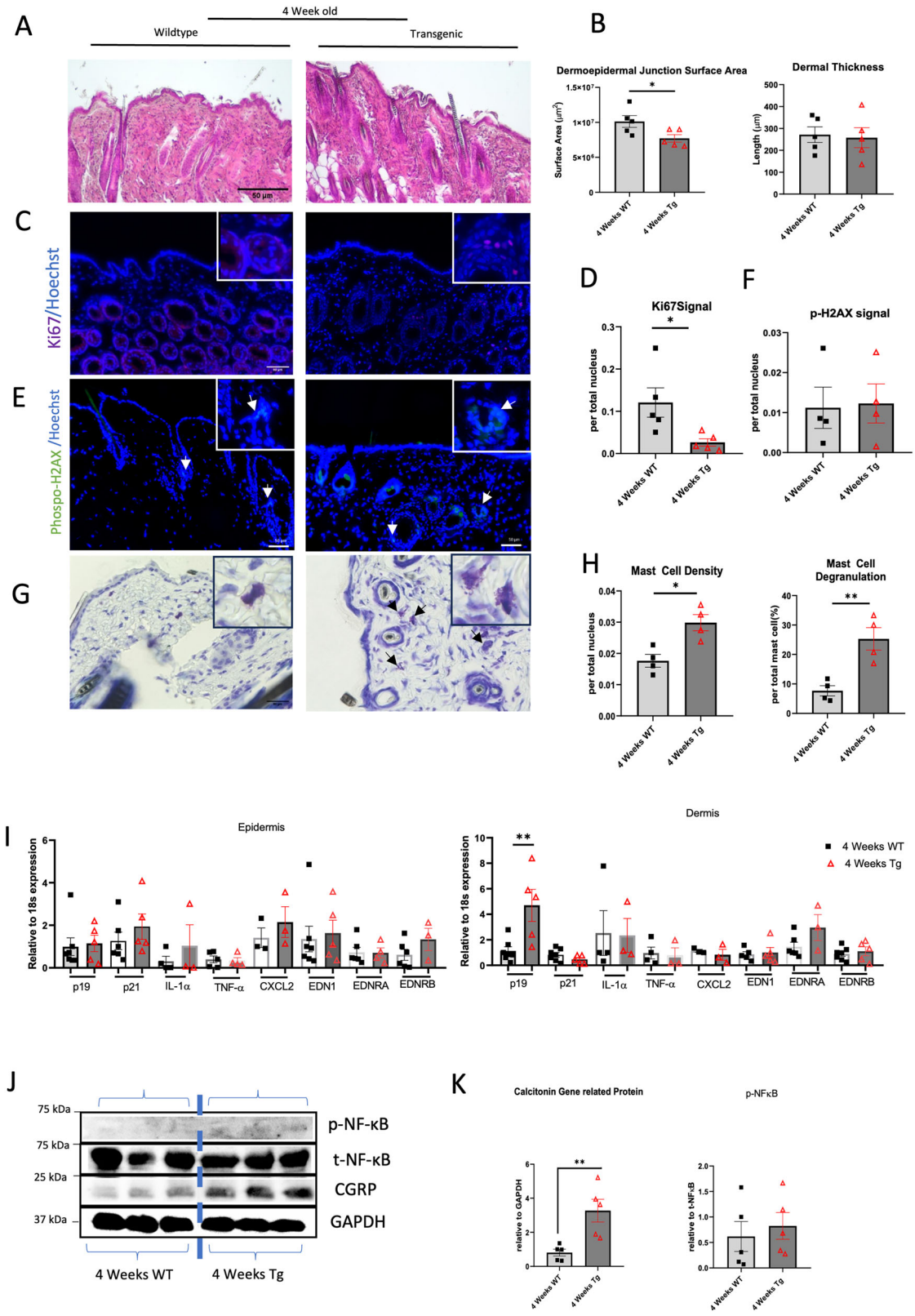

primary initiators of aging[25,46–48]. Targeting CGRP signaling with atogepant, a CGRP receptor antagonist, significantly reduced mast cell degranulation and attenuated skin aging markers, further supporting neuroimmune activation's critical role in skin aging[49]. However, in vitro atogepant exposure paradoxically increased TNF-α levels in fibroblasts, suggesting potential off-target effects that warrant further investigation.

While these findings support the involvement of vascular aging in skin deterioration, the long-term effects of targeting CGRP-mast cell signaling remain unclear[41]. Dexamethasone, a corticosteroid, effectively reduced CGRP expression and mast cell degranulation, further confirming SASP involvement in this pathway[35,50]. However, long-term steroid exposure is known to induce dermal atrophy, sebaceous gland degeneration, and

Fig. 4 | Younger TRF2DN-Tg mice showed some skin aging parameters and higher CGRP expression with comparable SASP expression. **A** Representative image of Masson's trichrome staining in 4-week-old WT or Tg mice. **B** Quantification of the dermoepidermal junction surface area of either WT or Tg mice in 10- and 40-week-old mice ($n = 5$ each). **C** Representative images of immunofluorescence staining for Ki67$^+$ proliferating cells in the dorsal skin of either WT or Tg 4-week-old mice. **D** Quantification of Ki67$^+$ cells in 4-week-old WT or Tg mice relative to the total nuclei ($n = 5$ each). **E** Representative image of immunofluorescence staining for the DNA-Damage response marker Phospo-H2AX$^+$ cells. Positive cells are indicated by white arrows. **F** Quantification of Phospo-H2AX$^+$ cells in WT and Tg mice relative to the total nucleus ($n = 4$ each). **G** Representative images of toluidine blue-staining in 4-week-old WT and Tg mice. **H** Quantification of mast cell density and degranulation (**G**) ($n = 3$). **I** Expression of CDK inhibitors, SASP factors, and endothelin-1 in the dermis and epidermis of either WT or Tg 4-week-old mice using RT-qPCR ($n = 5$–6 each). **J** Representative immunoblotting for CGRP and p-NFκB expression of whole skin lysate from 4-week-old WT or Tg mice. **K** Densitometric quantification for immunoblotting (**J**) ($n = 5$ each). A two-tailed Student's t-test was used to analyze the differences between two groups. #$P < 0.0001$; ***$P < 0.001$; **$P < 0.01$; *$P < 0.05$. Not significant ($P > 0.05$).

collagen loss, highlighting the need for alternative, more selective SASP-targeting strategies[50–52]. Specific IL-6 inhibition resulted in favorable attenuation of CGRP and subsequent mast cell degranulation, further confirm proposed pathway yet prolonged inhibition effect should be monitored closely.

Our findings offer significant implications for developing therapeutic interventions against skin aging. Higher mast cell density has been reported in aged dermis, accompanied by increased association with nerve fiber and degranulated morphology, although the molecular mechanism behind this increase is still largely unknown[25,53]. Our investigation targeting the EC-SASP-CGRP-mast cell axis confirmed similar findings in humans, especially regarding mast cells, while also representing a novel approach to delay or mitigate intrinsic skin aging by modulating the SASP- and CGRP-mediated neuro-immune interactions. Nevertheless, several questions remain unanswered, including whether vascular senescence influences other skin cell populations, such as fibroblasts or keratinocytes, independent of immune regulation. Furthermore, the interaction between systemic inflammaging and local vascular-neuroimmune signaling warrants further exploration. Additionally, the long-term safety and efficacy of CGRP-targeting therapies for dermatological applications require careful evaluation.

In conclusion, this study establishes a novel vascular-neuroimmune mechanism underlying intrinsic skin aging, linking EC senescence, CGRP signaling, and mast cell activation. These findings redefine vascular aging as an active driver, rather than a passive consequence, of skin aging and highlight potential therapeutic avenues for preventing age-related skin deterioration.

Materials and methods

Animal study

All researchers complied with relevant ethical regulations, and all experimental protocols were approved by the Ethics Review Committee for Experimentation of Kobe Pharmaceutical University (approval number 2024-003). All animal experiments adhered to ARRIVE (Animal Research: Reporting of In Vivo Experiments) guidelines. Premature endothelial senescent mice with endothelial-specific TRF2DN overexpression (VEcad-TRF2DN-TG) used in this study were generated with C57/BL6J background, as described previously[12]. Transgenic (Tg) mice were propagated as heterozygous animals by breeding wild-type (WT) C57/BL6J mice.

Mice were housed in the Kobe Pharmaceutical University animal facility at ~24 °C, 60% humidity, with a 12-hour light/12-hour dark cycle. All mice had ad libitum access to a normal chow diet (CRF-1, Charles River Laboratories International, Inc., Wilmington, MA, USA) and water.

Both male and female mice were used for experiments, with Tg mice compared to their WT littermates. For wound healing assay, experiment was conducted under ~2–2.5% isoflurane inhalation, and a 3 mm punch-biopsy wound was created on the right thigh. The wound area was documented daily until full closure. For mast cell stabilization studies, mice received weekly intraperitoneal (i.p.) injections of vehicle (corn oil) or quercetin (10 mg/kg body weight; Sigma-Aldrich #Q4951), flavonoid that have been reported to prevent mast cell degranulation[31]. For the calcitonin gene-related peptide (CGRP) inhibition study, mice received intradermal (i.d.) injections on the dorsal skin with vehicle (99.95% EtOH) or atogepant, CGRP receptor inhibitor[49] (3 mg/kg body weight; Selleck #1374248-81-3, JP) administered every three days for four doses. For the SASP inhibition study, daily intraperitoneal injections of either vehicle (corn oil) or dexamethasone steroid[35](5 mg/kg body weight; Sigma-Aldrich#D4902) were administered for 14 consecutive days. For IL-6 inhibition study, i.d. injection of vehicle (sterile PBS) or tocilizumab (5 mg/kg/body weight, Selleck #375823-41-9,JP) administered weekly for four doses[54,55]. All animals were anesthetized with isoflurane before termination by cervical dislocation.

Histological analysis

The dorsal skin of mice was harvested and fixed in 4% paraformaldehyde for 2 h, followed by either serial dehydration before embedding in paraffin blocks, or incubation overnight in 30% sucrose before embedding in optimal cutting temperature compound (Sakura Tissue Tek) frozen blocks. For stereological estimations, skin samples were collected using a 3-mm punch biopsy prior to paraffin embedding[56]. Paraffin-embedded blocks were sectioned into 4-μm slices and stained with Masson's trichrome, toluidine blue, or processed for immunostaining.

The dermoepidermal junction (DEJ) surface area was estimated using Masson's trichrome-stained slides as previously described[56]. Images were captured using a Keyence BZ-X800 microscope (Keyence, Osaka, Japan) at 11.1x objective lens magnification. Surface area estimations were performed using ImageJ software by randomly placing cycloid lines on captured images. Intersections between cycloids and the DEJ were counted, and dermal thickness was calculated from measurements at 10 random intersections per sample.

Immunostaining was performed on paraffin-embedded sections. After deparaffinization, slides underwent antigen retrieval using Antigen Unmasking Solution (Vector laboratories) at 90 °C for 10 min. Non-specific antigens were blocked with 5% donkey serum in PBS containing 0.1% Triton-X for 1 h. Primary antibodies used for immunostaining are listed in Supplementary data 3. Following incubation with primary antibodies, slides were washed and incubated with goat secondary antibodies labeled with Alexa Fluor 488, 594, or 647. Slides were then counterstained with Hoechst dye and mounted using 90% glycerol. To assess skin cell proliferation and DNA damage response markers (Ki67 and Phospho-histone H2AX, respectively), images of 10 random fields per sample were captured at x22.2 magnification. The number of positive cells was normalized to the total number of nuclei.

Mast cell density and degranulation were assessed using toluidine blue-stained sections. Mast cell density was evaluated at 22.2x magnification from 10 randomly captured high-power fields per sample and normalized to the total cell number. Degranulation was evaluated at 44.4x magnification from 50 randomly selected mast cells per sample. Confirmation of mast cell degranulation was assessed using tryptase immunostaining. Images of 100 randomly selected mast cell per sample were captured at 44.4x magnification.

Senescence-associated β-galactosidase (SA-β-Gal) activity was assessed using X-gal staining with modification[57]. Sections (6 μm) from OCT-

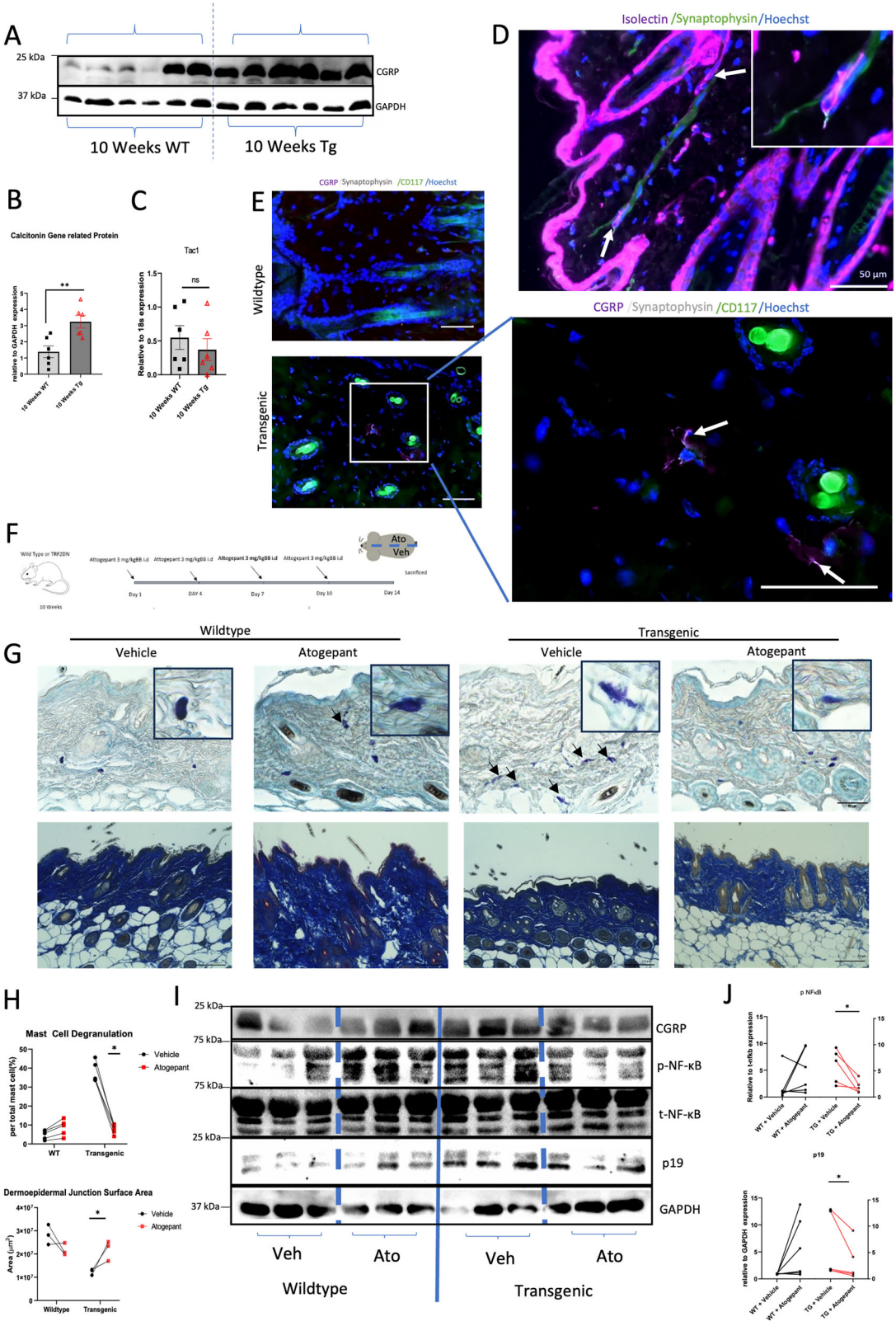

embedded blocks were fixed with 4% paraformaldehyde and incubated in X-gal solution (40 mM sodium phosphate, pH 6.0 + 5 mM potassium ferrocyanide + 5 mM potassium ferricyanide + 150 mM NaCl + 2 mM MgCl2 + 1 mg/mL X-Gal) in a light-protected container for 16 h at 37 °C. After three washes with PBS, slides were counterstained with nuclear fast red. Images were captured at 22.2× magnification from 10 random fields per sample, and the number of SA-β-Gal-positive cells was normalized to total cell numbers.

Intravital dermal collagen observation and confirmation

In vivo imaging of dermal collagen of the dorsal skin was performed as previously described[58]. Briefly, imaging was conducted using an upright

Fig. 5 | High CGRP levels induce mast cell degranulation, and CGRP inhibition alleviates skin aging in 10-week-old TRF2DN-Tg mice. A Representative immunoblotting for CGRP in whole skin lysate from 10-week-old WT or Tg mice. **B** Densitometry quantification for immunoblotting in (**A**) ($n = 6$ each). **C** Transcription analysis of dermal *Tac1* in 10-week-old WT and Tg mice ($n = 6$ each). **D** Representative image of Immunofluorescence staining of IB4$^+$ microvascular and synaptophysin dermal axon in WT 10-week-old mice. Close proximity of both tissues is marked by white arrows. **E** Representative images of immunofluorescence staining for CGRP, synaptophysin$^+$ dermal axons, and CD117$^+$ mast cells in WT or Tg 10-week-old mice. Colocalization of synaptophysin and CGRP is indicated by white arrows. **F** CGRP pathway inhibition using atogepant injection schematics. **G** Representative images of Masson's trichrome and toluidine blue staining in 10-week-old WT and Tg mice that received either atogepant or vehicle. **H** Quantification of the dermoepidermal junction surface area and mast cell degranulation (**F**) ($n = 4$ each). **I** Representative immunoblotting for CGRP, p-NFκB, and P19 expression of whole skin lysate from 10-week-old WT or Tg mice that receive either atogepant or vehicle. **J** Densitometric quantification for immunoblotting (**I**) ($n = 6$ each). Data are presented as mean ± SEM. A two-tailed Student's t-test was used to analyze the differences between two groups. A Paired Two-tailed Student's t-test was used for western blot densitometry. Two-way analysis of variance (ANOVA) with Sidak's post-hoc test was used to analyze differences between three or more groups. #$P < 0.0001$; ***$P < 0.001$; **$P < 0.01$; *$P < 0.05$. Not statistically significant ($P > 0.05$).

two-photon LSM 7 MP microscope system (Zeiss, Jena, Germany) coupled to a Ti:sapphire laser (Coherent Chameleon, Glasgow, UK). The laser was operated at an intensity of 12–18 mW at a wavelength of 860 nm, using a Zeiss 40x/1.0NA water-immersion objective lens. External non-descanned detectors equipped with 492/SP emission filters were employed to detect second harmonic generation (SHG) signals. Fluorescence signals were acquired from a 300 µm × 300 µm field to a depth of 100 µm, using vertical steps of 1 µm. Five randomly selected regions of interest (ROI) were imaged, and raw image data were processed using ZEN 2011software (Zeiss, Jena, Germany). Signal intensity was quantified using ImageJ FIJI software[31].

Collagen content was further confirmed using a hydroxyproline assay as previously described[59]. Whole skin samples (50 mg) were processed in RIPA buffer, and 100 µL aliquots of the diluted samples were placed into autoclavable screw-top tubes. After adding 100 µL 10 M NaOH, samples were autoclaved at 120 °C for 15 min. Solutions were neutralized using 100 µL 10 M HCl, and water was evaporated overnight in an incubator set at 70 °C. 625 µL Chloramine-T solution (0.05 M Chloramine-T in 74% v/v H2O, 26% v/v 2-propanol, 0.629 M NaOH, 0.140 M citric acid (monohydrate), 0.453 M sodium acetate (anhydrous), and 0.112 M acetic acid) was then added to dissolve the formed crystals, followed by the same amount of Erlich's reagent (1 M DMAB in 30% v/v HCl and 70% v/v 2-propanol) and incubation in a water bath at 65 °C. Samples were subsequently quenched and absorbance readings were taken at 500–550 nm using a Tecan Infinite 200 Pro microplate reader (Tecan, Mannedorf, Switzerland).

Unilateral surgical skin denervation

Unilateral back skin axotomy was conducted as described[60]. Briefly, 3 cm dorsal midline incision of the back skin was made after mice anesthetized. Dorsal cutaneous nerves (T3-T12) were exposed at both sides under stereomicroscope. Right nerves were dissected close to their anatomical entry while the left side was kept as sham control. Skin was closed using 6.0 non-tapered silk and sacrificed 10 days post-surgery.

Quantitative real-time PCR

Epidermal and dermal layers of skin were separated as described[61]. Approximately 100 mg of mouse dorsal skin was incubated epidermis-side-down in 3.8% ammonium thiocyanate solution for 20 min. Tissue layers were then carefully separated under a stereomicroscope, and the respective epidermal and dermal samples were immersed in RNAiso Plus solution (Takara, Shiga, Japan). Tissues were homogenized using a PT1200E homogenizer (Kinematica, Switzerland), and the homogenates were centrifuged at 15,000 × *g* at 4 °C for 15 min. Supernatants were purified using the NucleoSpin RNA Clean-Up kit (Macherey-Nagel, Duren, Germany). cDNA synthesis was performed from approximately 1 µg of RNA using PrimeScript RT Reagent with gDNA-eraser (Takara, Shiga, Japan). Quantitative real-time PCR (qPCR) was conducted using the TB Green Premix Ex Taq II kit (Takara Bio, Shiga, Japan) on a LightCycler96 system (Roche Applied BioScience). Gene expression was normalized against 18S rRNA levels and analyzed using the $2^{-\Delta\Delta CT}$ method. Primers used in these experiments are listed in Supplementary data 2.

Protein extraction and immunoblotting

Antibodies used for immunoblotting are listed in Supplementary data 3. Skin tissue, dorsal-root ganglion, and sciatic samples (25–50 mg) were homogenized using a Dounce homogenizer in RIPA buffer supplemented with protease and phosphatase inhibitors. Protein concentrations were determined using the Bio-Rad Protein assay (Bio-Rad, Hercules, CA, USA), equalized by dilution with sample buffer (0.0625 M Tris-HCl pH6.8, 2% SDS,10% glycerol, 2% 2 -mercaptoethanol, and denatured at 95 °C for 5 min. For conditioned media-derived sample, non-reducing sample buffer (125 mM Tris-HCL, pH 6.8, 4% SDS, 20% glycerol, 001% bromophenol blue) was used without denaturation process. Lysates were electrophoresed on 15% sodium dodecyl sulfate-polyacrylamide gels and transferred onto nitrocellulose membranes. Membranes were blocked with TBS-T containing 5% skim milk to prevent non-specific binding and incubated overnight at 4 °C with primary antibodies diluted in Can Get Signal Solution (Toyobo, Osaka, Japan). After thorough washing with TBS-T, membranes were incubated with the appropriate secondary antibodies. Chemiluminescent signals were detected using Amersham ECL (Cytiva, MA, USA) and visualized with a ChemiDoc XRS+ imaging system (Bio-Rad; Hercules, CA, USA). Signal intensities were normalized against GAPDH expression, and results expressed in arbitrary units.

Enzyme-linked immunosorbent assay (ELISA)

ELISA kits for IgE (BioLegend, CA, USA) and IL-1β (Abcam, UK) were used according to the manufacturer's instructions to analyze serum samples from 10-week-old WT and transgenic mice.

Primary cell isolation and culture

Mouse dermal fibroblasts were isolated as previously described[62]. Dorsal skin from WT mice was incubated overnight at 4 °C with the epidermal side facing downward in Dispase II (100 U/mL; Fujifilm Wako, Japan). Epidermal and dermal layers were separated under sterile conditions, and the dermal tissue was minced and digested with Type-IV Collagenase (1 mg/mL; Worthington Biochemical, NJ, USA) supplemented with 1 mg/mL BSA at 37 °C for 1 h. The cell suspension was centrifuged, and pellets were resuspended in low-glucose DMEM supplemented with 10% FBS and 1% ABAM under 5% CO_2 and 37 °C condition. Cells were cultured until reaching ~90% confluency, and cells at passage two were used for experiments.

Dermal endothelial cells from WT and transgenic mice were isolated using the same procedure, except that the cells were cultured in Humedia-EG2 medium supplemented with 10% FBS and 1% ABAM. Cell suspensions were filtered through a 70 µm cell strainer (Falcon, Corning), cultured to ~90% confluency, and the conditioned media were collected and stored at −80 °C before use. Passage number-two cells were used in subsequent experiments.

Peritoneal-derived mast cell isolation was conducted as described[63] on 10-week-old WT mice. Following anesthesia, ventral skin of mouse was removed using blunt edge scissors while avoiding damaging peritoneum. Seven mL of ice-cold RPMI medium and 5 mL of air was carefully injected into the peritoneal cavity using 10 mL syringe equipped with 27 G needle in

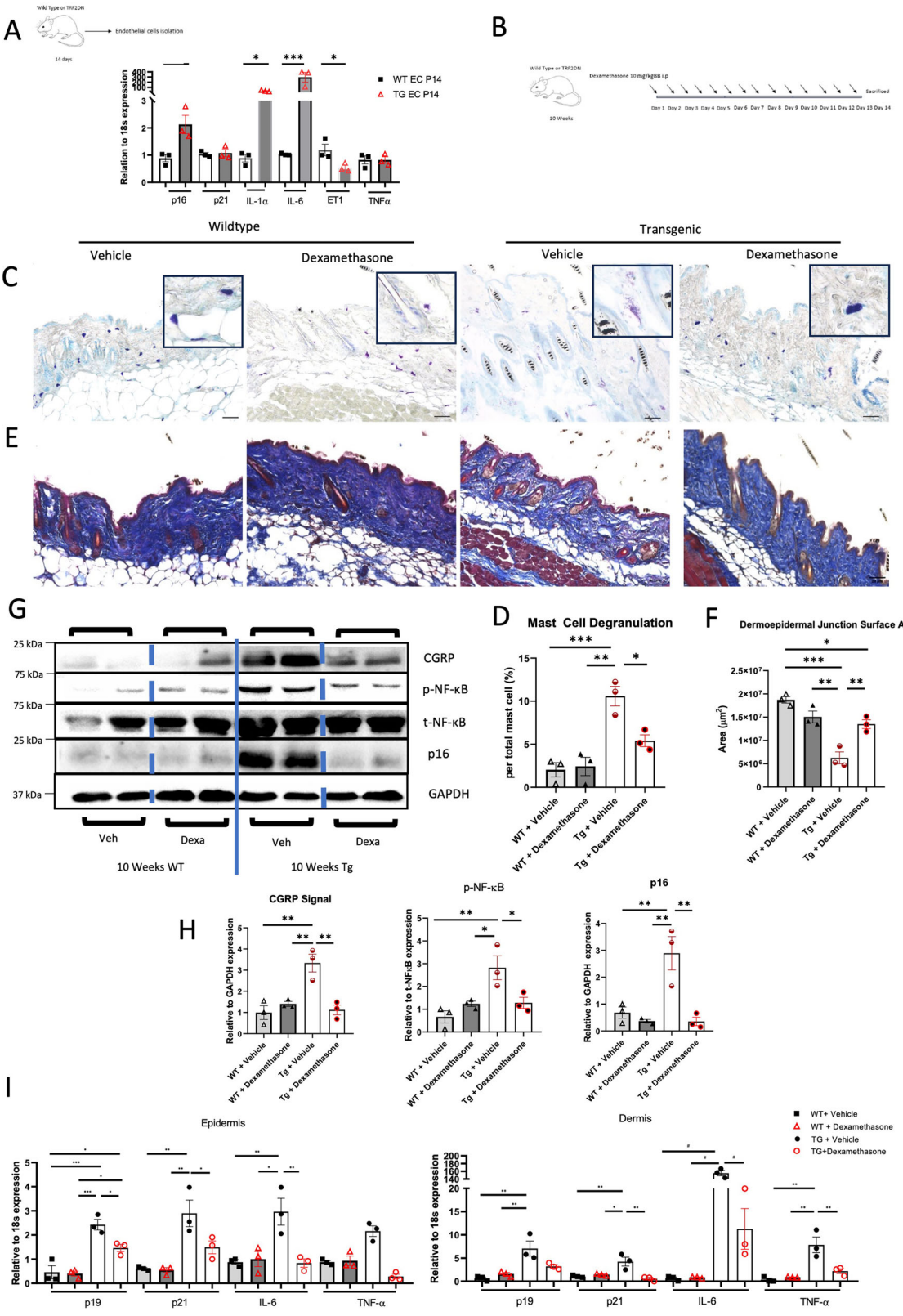

the region of linea alba without touching internal organs. Mouse was shaken gently for 1 min to detach peritoneal cells. Syringe was reused and equipped with a new 20 G needle before injected into the cavity to aspirate the medium as much as possible (typically 5–6 mL). Cell suspension was transferred into new tubes followed by centrifugation at 300 g for 5 min. Cells was resuspended in RPMI medium supplemented with 20% FBS, 10 ng/mL Interleukin (IL)-3 (MedChemExpress HY-P70576), and 30 ng/mL Stem Cell Factor/SCF (MedChemExpress HY-P70528). Medium was changed 48 h after isolation while subculturing conducted at day 9. Second passaged cells were used in the experiment.

Fig. 6 | SASP from progeroid ECs induces CGRP overexpression, which is attenuated by dexamethasone treatment. A Transcription level analysis of CDKIs and SASP expression in endothelial cells isolated from 4-week-old Tg or WT mice ($n = 3$ biologically independent cells per group). **B** SASP inhibition using dexamethasone injection schematic. **C** Representative images of toluidine blue staining in 10-week-old WT and Tg mice that received either dexamethasone or vehicle. **D** Quantification of mast cell degranulation (**D**) ($n = 3$ each). **E** Representative images of Masson's trichrome staining in 10-week-old WT and Tg mice that received either dexamethasone or vehicle. **F** Quantification of the dermoepidermal junction surface area (**F**) ($n = 3$ each). **G** Representative immunoblotting for CGRP, p-NFκB, and P16 expression of whole skin lysate from 10-week-old WT or Tg mice, which received either dexamethasone or vehicle. **H** Densitometry quantification for immunoblotting in (**H**) ($n = 3$ each). **I** Transcription analysis of CDK inhibitors and SASP factors expression in the dermis and epidermis of either WT or Tg 10-week-old mice which received dexamethasone or vehicle ($n = 3$ each) Two-way ANOVA with Tukey's post hoc test was used to analyze the differences between three or more groups. #$P < 0.0001$; ***$P < 0.001$; **$P < 0.01$; *$P < 0.05$. Not statistically significant ($P > 0.05$).

Statistics and reproducibility

All data are expressed as mean ± SEM. with individual data points shown in all plots to display full data distribution. For each analysis, the sample size (n) is specified in the figure legends. Differences between two independent groups were evaluated using a two-tailed unpaired t-test, whereas data derived from the same animals were assessed using a paired t-test. Differences involving more than two groups were analyzed using two-way ANOVA followed by Sidak's post-hoc test. Statistical significance was set at $P < 0.05$ and exact P values are reported in the Supplementary data 1. For all the data, experiments were replicated for 2–3 independent times. All statistical analyses were conducted using GraphPad Prism 10.4 (GraphPad Software Inc., Boston, MA, USA).

Reporting summary

Further information on research design is available in the Nature Portfolio Reporting Summary linked to this article.

Data availability

The authors declare that all data supporting the findings of this study are available within the paper and its Supplementary Information files. The source data underlying Figs. 1C, E, G, I, J, 2B, D, F, G, I, 3B, D, F, I, K, 4 B, D, F, H, I, K, 5B, G, I, 6A, D, F, H, I as well as uncropped and unedited blot image are provided as the Supplementary data 1 File.

Received: 6 April 2025; Accepted: 18 October 2025;
Published online: 26 November 2025

References

1. Durai, P., Thappa, D., Kumari, R. & Malathi, M. Aging in elderly: Chronological versus photoaging. *Indian J. Dermatol.* **57**, 343 (2012).
2. Cines, D. B. et al. Endothelial cells in physiology and in the pathophysiology of vascular disorders. *Blood* **91**, 3527–3561 (1998).
3. Jia, G., Aroor, A. R., Jia, C. & Sowers, J. R. Endothelial cell senescence in aging-related vascular dysfunction. *Biochim. Biophys. Acta Mol. Basis Dis.* **1865**, 1802–1809 (2019).
4. Herranz, N. & Gil, J. Mechanisms and functions of cellular senescence. *J. Clin. Investig.* **128**, 1238–1246 (2018).
5. Han, Y. & Kim, S. Y. Endothelial senescence in vascular diseases: current understanding and future opportunities in senotherapeutics. *Exp. Mol. Med.* **55**, 1–12 (2023).
6. Childs, B. G., Durik, M., Baker, D. J. & van Deursen, J. M. Cellular senescence in aging and age-related disease: from mechanisms to therapy. *Nat. Med.* **21**, 1424–1435 (2015).
7. Lecot, P., Alimirah, F., Desprez, P.-Y., Campisi, J. & Wiley, C. Context-dependent effects of cellular senescence in cancer development. *Br. J. Cancer* **114**, 1180–1184 (2016).
8. Harvey, A., Montezano, A. C. & Touyz, R. M. Vascular biology of ageing-Implications in hypertension. *J. Mol. Cell Cardiol.* **83**, 112–121 (2015).
9. Lin, T.-C. et al. Comprehensive assessment and management of hypertension in elderly patients: Addressing frailty and target organ damage. *J. Formosan Med. Assoc.* https://doi.org/10.1016/j.jfma.2024.10.023 (2024).
10. Barinda, A. J. et al. Endothelial progeria induces adipose tissue senescence and impairs insulin sensitivity through senescence associated secretory phenotype. *Nat. Commun.* **11**, 481 (2020).
11. Kawauchi, S. et al. Gliovascular interface abnormality in mice with endothelial cell senescence. *Glia* **71**, 467–479 (2023).
12. Ramadhiani, R. et al. Endothelial cell senescence exacerbates pulmonary hypertension by inducing juxtacrine Notch signaling in smooth muscle cells. *iScience* **26**, 106662 (2023).
13. Walker, M. Human skin through the ages. *Int J. Pharm.* **622**, 121850 (2022).
14. Farage, M. A., Miller, K. W., Elsner, P. & Maibach, H. I. Characteristics of the Aging Skin. *Adv. Wound Care* **2**, 5–10 (2013).
15. Zhang, S. & Duan, E. Fighting against skin aging: the way from bench to bedside. *Cell Transplant.* **27**, 729–738 (2018).
16. Blume-Peytavi, U. et al. Age-associated skin conditions and diseases: current perspectives and future options. *Gerontologist* **56**, S230–S242 (2016).
17. Fukumoto, T., Shimosawa, T., Yakabe, M., Yoshida, S. & Yoshida, Y. Recent advances in biomarkers for senescence: Bridging basic research to clinic. *Geriatr. Gerontol. Int* **25**, 139–147 (2025).
18. Li, K. N. et al. Skin vasculature and hair follicle cross-talking associated with stem cell activation and tissue homeostasis. *Elife* **8**, e45977 (2019).
19. Sanchez, B. et al. Impact of human dermal microvascular endothelial cells on primary dermal fibroblasts in response to inflammatory stress. *Front. Cell Dev. Biol.* **7** (2019).
20. Agrawal, R., Hu, A. & Bollag, W. B. The skin and inflamm-aging. *Biology* **12**, 1396 (2023).
21. Zakar-Polyák, E., Csordas, A., Pálovics, R. & Kerepesi, C. Profiling the transcriptomic age of single-cells in humans. *Commun. Biol.* **7**, 1397 (2024).
22. Kupper, T. S. & Fuhlbrigge, R. C. Immune surveillance in the skin: mechanisms and clinical consequences. *Nat. Rev. Immunol.* **4**, 211–222 (2004).
23. Galli, S. J. & Tsai, M. IgE and mast cells in allergic disease. *Nat. Med.* **18**, 693–704 (2012).
24. Sarchio, S. N. E., Kok, L., O'Sullivan, C., Halliday, G. M. & Byrne, S. N. Dermal mast cells affect the development of sunlight-induced skin tumours. *Exp. Dermatol* **21**, 241–248 (2012).
25. Pilkington, S. M., Barron, M. J., Watson, R. E. B. & Griffiths, C. E. M. & Bulfone-Paus, S. Aged human skin accumulates mast cells with altered functionality that localize to macrophages and vasoactive intestinal peptide-positive nerve fibres. *Br. J. Dermatol.* **180**, 849–858 (2019).
26. Boros, M., Szalay, L. & Kaszaki, J. Endothelin-1 induces mucosal mast cell degranulation and tissue injury via ETA receptors. *Clin. Sci.* **103**, 31S–34S (2002).
27. Gallenga, C. E. et al. Interleukin-1 family cytokines and mast cells: activation and inhibition. *J. Biol. Regul. Homeost. Agents* **33**, 1–6 (2019).
28. Hultner, L. & Ehrenreich, H. Mast cells and endothelin-1: a life-saving biological liaison? *Trends Immunol.* **26**, 235–238 (2005).

29. Galli, S. J., Gaudenzio, N. & Tsai, M. Mast cells in inflammation and disease: recent progress and ongoing concerns. *Annu Rev. Immunol.* **38**, 49–77 (2020).
30. Burton, D. G. A. & Krizhanovsky, V. Physiological and pathological consequences of cellular senescence. *Cell. Mol. Life Sci.* **71**, 4373–4386 (2014).
31. Weng, Z. et al. Quercetin is more effective than cromolyn in blocking human mast cell cytokine release and inhibits contact dermatitis and photosensitivity in humans. *PLoS One* **7**, e33805 (2012).
32. Weidner, C. et al. Acute effects of substance P and calcitonin gene-related peptide in human skin–a microdialysis study. *J. Investig. Dermatol.* **115**, 1015–1020 (2000).
33. Gibbins, I. L. et al. Co-localization of calcitonin gene-related peptide-like immunoreactivity with substance P in cutaneous, vascular and visceral sensory neurons of guinea pigs. *Neurosci. Lett.* **57**, 125–130 (1985).
34. Russell, F. A., King, R., Smillie, S.-J., Kodji, X. & Brain, S. D. Calcitonin gene-related peptide: physiology and pathophysiology. *Physiol. Rev.* **94**, 1099–1142 (2014).
35. Laberge, R. et al. Glucocorticoids suppress selected components of the senescence-associated secretory phenotype. *Aging Cell* **11**, 569–578 (2012).
36. Jimenez-Andrade, J. M. et al. Vascularization of the dorsal root ganglia and peripheral nerve of the mouse: implications for chemical-induced peripheral sensory neuropathies. *Mol. Pain.* **4**, 10 (2008).
37. Yorek, M. A. Vascular Impairment of Epineurial Arterioles of the Sciatic Nerve: Implications for Diabetic Peripheral Neuropathy. *Rev. Diabet. Stud.* **12**, 13–28 (2015).
38. Lin, C.-Y. et al. Sex- and age-dependent skin mechanics—a detailed look in mice. *Acta Biomater.* **175**, 106–113 (2024).
39. Rolas, L. et al. Senescent endothelial cells promote pathogenic neutrophil trafficking in inflamed tissues. *EMBO Rep.* **25**, 3842–3869 (2024).
40. Voss, M., Kotrba, J., Gaffal, E., Katsoulis-Dimitriou, K. & Dudeck, A. Mast cells in the skin: defenders of integrity or offenders in inflammation? *Int. J. Mol. Sci.* **22**, 4589 (2021).
41. Raddant, A. C. & Russo, A. F. Calcitonin gene-related peptide in migraine: intersection of peripheral inflammation and central modulation. *Expert Rev. Mol. Med* **13**, e36 (2011).
42. Neeb, L. et al. IL-1β Stimulates COX-2 Dependent PGE2 Synthesis and CGRP Release in Rat Trigeminal Ganglia Cells. *PLoS One* **6**, e17360 (2011).
43. Ebbinghaus, M. et al. Interleukin-6-dependent influence of nociceptive sensory neurons on antigen-induced arthritis. *Arthritis Res. Ther.* **17**, 334 (2015).
44. Kim, Y. J. & Granstein, R. D. Roles of calcitonin gene-related peptide in the skin, and other physiological and pathophysiological functions. *Brain Behav. Immun. Health* **18**, 100361 (2021).
45. Assas, B. M., Pennock, J. I. & Miyan, J. A. Calcitonin gene-related peptide is a key neurotransmitter in the neuro-immune axis. *Front. Neurosci.* **8**, 23 (2014).
46. Schültke, E., Kamencic, H., Skihar, V. M., Griebel, R. & Juurlink, B. Quercetin in an animal model of spinal cord compression injury: correlation of treatment duration with recovery of motor function. *Spinal Cord.* **48**, 112–117 (2010).
47. Bientinesi, E. et al. Doxorubicin-induced senescence in normal fibroblasts promotes in vitro tumour cell growth and invasiveness: the role of Quercetin in modulating these processes. *Mech. Ageing Dev.* **206**, 111689 (2022).
48. Hu, J. et al. Epidermal mechanical scratching-induced ros exacerbates the itch-scratch cycle via TRPA1 activation on mast cells in atopic dermatitis. *J. Investig. Dermatol.* https://doi.org/10.1016/j.jid.2024.12.026 (2025).
49. Ailani, J. et al. Atogepant for the preventive treatment of migraine. *N. Engl. J. Med.* **385**, 695–706 (2021).
50. Kang, W., Ha, Y., Jung, Y., Lee, H. & Park, T. Nerol mitigates dexamethasone-induced skin aging by activating the Nrf2 signaling pathway in human dermal fibroblasts. *Life Sci.* **356**, 123034 (2024).
51. Baida, G. et al. Deletion of the glucocorticoid receptor chaperone FKBP51 prevents glucocorticoid-induced skin atrophy. *Oncotarget* **9**, 34772–34783 (2018).
52. Agarwal, S., Mirzoeva, S., Readhead, B., Dudley, J. T. & Budunova, I. PI3K inhibitors protect against glucocorticoid-induced skin atrophy. *EBioMedicine* **41**, 526–537 (2019).
53. Abdel Hafez, S. M. N. Age related changes in the dermal mast cells and the associated changes in the dermal collagen and cells: A histological and electron microscopy study. *Acta Histochem.* **121**, 619–627 (2019).
54. Tu, Y. et al. Tocilizumab attenuates choroidal neovascularization by regulating macrophage polarization through the IL-6R/STAT3/VEGF pathway. *Heliyon* **10**, e27893 (2024).
55. Hudobenko, J., Chauhan, A. & McCullough, L. Abstract 28: inhibition of interleukin-6 signaling with tocilizumab ameliorates ischemic stroke damage in aged male and female mice. *Stroke* **49** (2018).
56. Kamp, S. et al. Stereological estimation of epidermal volumes and dermo-epidermal surface area in normal skin. *Dermatology* **223**, 131–139 (2011).
57. Idelfonso-García, O. G. et al. Protocol to detect senescence-associated β-galactosidase and immunoperoxidase activity in fresh-frozen murine tissues. *STAR Protoc.* **5**, 103009 (2024).
58. Yasui, T. et al. In vivo observation of age-related structural changes of dermal collagen in human facial skin using collagen-sensitive second harmonic generation microscope equipped with 1250-nm mode-locked Cr:Forsterite laser. *J. Biomed. Opt.* **18**, 031108 (2012).
59. Cissell, D. D., Link, J. M., Hu, J. C. & Athanasiou, K. A. A modified hydroxyproline assay based on hydrochloric acid in Ehrlich's solution accurately measures tissue collagen content. *Tissue Eng. Part C. Methods* **23**, 243–250 (2017).
60. Siebenhaar, F. et al. Mast cell–driven skin inflammation is impaired in the absence of sensory nerves. *J. Allergy Clin. Immunol.* **121**, 955–961 (2008).
61. Clemmensen, A. et al. Extraction of high-quality epidermal RNA after ammonium thiocyanate-induced dermo-epidermal separation of 4 mm human skin biopsies. *Exp. Dermatol.* **18**, 979–984 (2009).
62. Kisiel, M. A. & Klar, A. S. Isolation and culture of human dermal fibroblasts. in 71–78 https://doi.org/10.1007/978-1-4939-9473-1_6 (2019).
63. Tsvilovskyy, V., Solis-Lopez, A., Öhlenschläger, K. & Freichel, M. Isolation of peritoneum-derived mast cells and their functional characterization with Ca2+-imaging and Degranulation Assays. *J. Vis. Experim.* https://doi.org/10.3791/57222 (2018).

Acknowledgements

We thank Pranindya Rinastiti, Aditya Adinata, Arinal Chairul Achyar, Novia Nurul Faizah, Sagita Mega Sekar Kencana, and Saiful Hidayat for their excellent technical assistance. We thank Ria Lupitasari for excellent graphical abstract.

Author contributions

S.A.W. performed most of the experiments. S.A.W., G.R.T.R., T.F. and N.E. performed the data analyses and wrote the manuscript. T.H. and Y.S. performed in vivo microscopy and analyses. K.I. generated the transgenic mice. T.F., H.O., K.I.H. and N.E. conceived and supervised overall experiment.

Competing interests

The authors declare no competing interests.

Additional information

Supplementary information The online version contains supplementary material available at https://doi.org/10.1038/s42003-025-09097-2.

Correspondence and requests for materials should be addressed to Noriaki Emoto.

Peer review information *Communications Biology* thanks the anonymous reviewers for their contribution to the peer review of this work. Primary Handling Editor: Dario Ummarino. A peer review file is available.